J. Fluid Mech. (2024), *vol*. 987, R2, doi:10.1017/jfm.2024.378

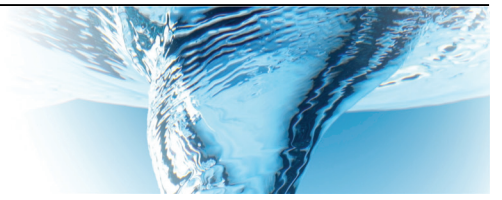

Jetting enhancement from wall-proximal cavitation bubbles by a distant wall

Qingyun Zeng[1,2], A-Man Zhang[1,2,†], Beng Hau Tan[3], Hongjie An[4] and Claus-Dieter Ohl[5,†]

[1]College of Shipbuilding Engineering, Harbin Engineering University, Harbin 150001, PR China

[2]Nanhai Institute of Harbin Engineering University, Sanya 572024, PR China

[3]Shenzhen Institute for Advanced Study, University of Electronic Science and Technology of China, Shenzhen 518109, PR China

[4]Queensland Micro and Nanotechnology Centre, Griffith University, Nathan, QLD 4111, Australia

[5]Department for Soft Matter, Otto-von-Guericke-University Magdeburg, Magdeburg 39016, Germany

(Received 22 February 2024; revised 20 March 2024; accepted 10 April 2024)

An additional distant wall is known to highly alter the jetting scenarios of wall-proximal bubbles. Here, we combine high-speed photography and axisymmetric volume of fluid (VoF) simulations to quantitatively describe its role in enhancing the micro-jet dynamics within the directed jet regime (Zeng *et al.*, *J. Fluid Mech.*, vol. 896, 2020, A28). Upon a favourable agreement on the bubble and micro-jet dynamics, both experimental and simulation results indicate that the micro-jet velocity increases dramatically as η decreases, where $\eta = H/R_{max}$ is the distance between two walls H normalized by the maximum bubble radius R_{max}. The mechanism is related to the collapsing flow, which is constrained by the distant wall into a reverse stagnation-point flow that builds up pressure near the bubble's top surface and accelerates it into micro-jets. We further derive an equation expressing the micro-jet velocity $U_{jet} = 87.94\gamma^{0.5}(1 + (1/3)(\eta - \lambda^{1.2})^{-2})$, where $\gamma = d/R_{max}$ is the stand-off distance to the proximal wall with d the distance between the initial bubble centre and the wall, $\lambda = R_{y,m}/R_{max}$ with $R_{y,m}$ the distance between the top surface and the proximal wall at the bubble's maximum expansion. Viscosity has a minimal impact on the jet velocity for small γ, where the pressure buildup is predominantly influenced by geometry.

Key words: bubble dynamics, cavitation

† Email addresses for correspondence: zhangaman@hrbeu.edu.cn, claus-dieter.ohl@ovgu.de

1. Introduction

The collapse of a wall-proximal cavitation bubble results in a micro-jet that pierces the bubble, morphs it into a torus, and the jet flow impacts onto the boundary, and then spreads along the boundary (Plesset & Chapman 1971; Lauterborn & Bolle 1975; Zhang *et al.* 2023). This rich fluid mechanics occurs in a brief period of time, including ring vortices formation and spreading along or away from the wall (Reuter *et al.* 2017), creation of large wall-normal and tangential shear stresses through the jet impact and its spreading (Dijkink & Ohl 2008; Zeng, An & Ohl 2022). Depending on the application, these flows may be unwanted due to the destructive effect or exploited for their benefit, e.g. for ultrasonic cleaning, drug delivery, histotripsy, lithotripsy and cavitation peening.

Recent experiment (Reuter & Ohl 2021) and simulation (Lechner *et al.* 2020) demonstrated that a micro-jet could be either a needle-type or a regular jet depending on the stand-off distance γ. Under atmospheric pressure, simulations and experiments find a needle jet velocity of the order 1000 m s^{-1}, yet it is extremely thin and develops only for $\gamma < 0.2$. In contrast, the regular jet has a speed of the order of 80 m s^{-1} that increases slowly with γ. The micro-jet shape and velocity are dependent on the particular flow conditions, where acoustic (Rosselló *et al.* 2018) and electric fields (Taleghani *et al.* 2023), bubble interaction (Han *et al.* 2015), and the presence of more than one boundary (Zeng, Gonzalez-Avila & Ohl 2020) have been reported to affect the velocity.

A recent study highlighted that an additional distant wall leads to more intricate bubble dynamics, unveiling three distinct jetting phenomena: transferred, double and directed jets (Zeng *et al.* 2020). The conditions for the formation of different jets were studied in detail, combining high-speed photography and Computational Fluid Dynamics (CFD) simulations, taking into account the stand-off distance γ from the proximal wall and the normalized gap height $\eta = H/R_{max}$ as crucial parameters. This finding opens avenues for manipulating jets, as the direction and strength of the jet can be tuned for specific applications based on the identified parameters.

Here we focus on the directed jet regime (Zeng *et al.* 2020), where the bubble neither splits (Ogasawara *et al.* 2015; Seki *et al.* 2015) nor translates (Gonzalez-Avila *et al.* 2020) to the distant wall. The aim is to quantitatively elucidate the micro-jet enhancement by the distant wall. We combine high-speed photography at up to 500 000 frames per second (f.p.s.) and compressible volume of fluid (VoF) simulations with high spatio-temporal resolution to investigate the details of the flow and derive an analytic expression for the jet velocity.

2. Experiments and simulation

Figures 1(*a*) and 1(*b*) sketch the geometry and introduce the coordinates and parameters of the problem. The experimental set-up is similar to Zeng *et al.* (2020). In the experiment, a laser pulse from a *Q*-switched Nd: YAG laser (Litron Nano S, 532 nm wavelength, 6 ns pulse duration) is focused into the deionized water at a distance of d to a no-slip proximal wall to nucleate the cavitation bubble. The distant wall is located at a distance of H from the proximal wall. Both walls are made of glass. A high-speed camera (Shimadzu Hypervision HPV-2) connected to a macro lens (Nikor) and an adapter ring (Nikon, model PB-6) records the bubble dynamics. A weakly diffused light pulse from a strobe light (Sunpak 3075G, 4.4 ms flash duration) illuminates the scene. The camera operates at a frame rate of 500 000 f.p.s. and a resolution of 18 μm per pixel. A delay generator (Quantum, 9520 series) controls the synchronization of the camera, the pulsed laser and the strobe. Experiments are conducted under atmospheric pressure, i.e. $p_\infty = 101\,325$ Pa.

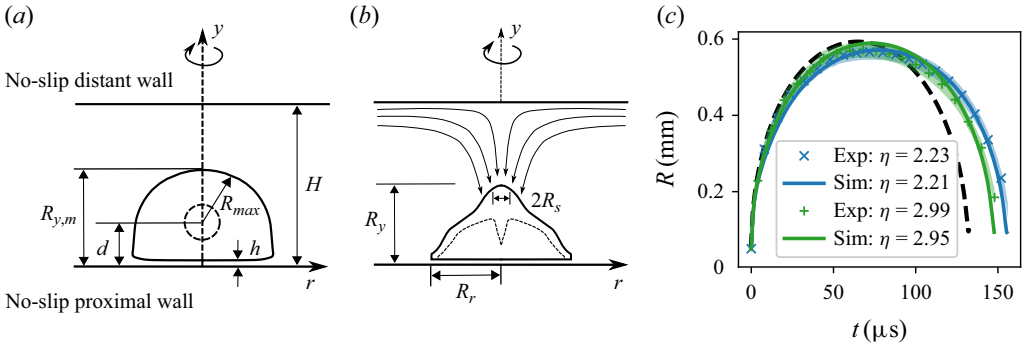

Figure 1. (*a*) Schematic diagram of the problem and parameters. The dashed circle indicates the nucleated bubble. The solid hat-shaped curve represents a bubble at its maximum expansion with a spherical equivalent radius R_{max}. The distant wall is located at a distance H from the proximal wall. The liquid film between the bubble's lower wall and the boundary has a thickness of h. (*b*) Schematic diagrams at the moments prior to (solid line) and immediately after (dashed line) the formation of the micro-jet. Here R_s and R_r indicate the radius of the bubble's apex and the bubble's radial extension, respectively. Curved arrows sketch the reverse stagnation-point flow during the collapse. (*c*) Comparison of experiments and simulation on bubble radii as a function of time for two selected cases with different $\eta = 2.23$ and $\eta = 2.99$ but similar stand-off distance $\gamma \approx 0.48$; areas coded by light colour indicate regions of experimental uncertainties. Black dashed line is the numerical bubble dynamics for the unconfined case, $\eta \to \infty$.

The bubble is created with a focused laser pulse that induces a dielectric breakdown in the liquid. Once formed, the laser-induced cavitation bubble expands and collapses violently, and continues to oscillate a few times. Yet most of the potential energy of the bubble is transferred into the liquid during the first cycle, i.e. when the micro-jet is formed. During this period, the cavitation bubble content can be treated as a gas bubble with a polytropic equation of state (EOS) and the liquid is modelled as a Tait liquid to account for compressibility (Koch *et al.* 2016).

We define a volume fraction of the liquid phase α, whose evolution is solved by the transport equation:

$$\frac{\partial \alpha}{\partial t} + \nabla \cdot (\alpha \boldsymbol{u}) + \nabla \cdot (\alpha(1-\alpha)\boldsymbol{U_r}) = \alpha(1-\alpha)\left(\frac{\psi_g}{\rho_g} - \frac{\psi_l}{\rho_l}\right)\frac{\mathrm{D}p}{\mathrm{D}t} + \alpha \nabla \cdot \boldsymbol{u}, \tag{2.1}$$

where t is time and $\boldsymbol{u}$ is the flow velocity. The compressibilities $\psi = \mathrm{D}\rho/\mathrm{D}p$ of both phases are modelled based on their EOS with fluid density ρ and the flow pressure p. Subscripts g and l denote the gas and liquid phases, respectively. Here $\boldsymbol{U_r}$ is an artificial compressible term obtained from the velocity difference between two phases, which enables tuning of the sharpness of the interface (Rusche 2003).

Here, the heat and mass transfer are neglected (Koch *et al.* 2016). Thus, the flow is governed by the equations of continuity and momentum:

$$\frac{\partial \rho}{\partial t} + \nabla \cdot (\rho \boldsymbol{u}) = 0, \tag{2.2}$$

$$\frac{\partial \rho \boldsymbol{u}}{\partial t} + \nabla \cdot (\rho \boldsymbol{u}\boldsymbol{u}) = -\nabla p + \nabla \cdot \boldsymbol{\tau} + \boldsymbol{f_\delta}, \tag{2.3}$$

where $\boldsymbol{\tau} = \mu[\nabla \boldsymbol{u} + \nabla \boldsymbol{u}^T - \frac{2}{3}(\nabla \cdot \boldsymbol{u})\boldsymbol{I}]$ is the viscous stress tensor calculated based on the identity tensor $\boldsymbol{I}$ and the dynamic viscosity μ. The surface tension term $\boldsymbol{f_\delta}$ is accounted for using the continuous-surface-force (CSF) method (Brackbill, Kothe & Zemach 1992).

Due to the axisymmetric nature of the problem, the domain is simplified as a wedge. To achieve a well-resolved flow and meanwhile keep the computational efficiency, we used a locally and recursively refined mesh and kept the cell size to 1.5 μm in the area where the bubble is located. To resolve the boundary-layer flow, the near-wall region is further refined to a cell size of 50 nm. Both walls are modelled as no-slip walls. The ambient pressure $p_\infty = 101\,325$ Pa is applied at the exit of the gap. See Zeng *et al.* (2018, 2020); Reese *et al.* (2022) for further details on the numerical implementation.

3. Bubble dynamics and micro-jet formation

In the simulation, the explosive growth of a laser-induced bubble is achieved by initiating a high-pressure gas pocket with an initial radius $R_0 = 50$ μm at $t = 0$. The initial pressure of the bubble p_0 is the only free parameter and is adjusted to match the experimental period of growth and collapse of the bubble. Figure 1(*c*) compares the experimental and numerical results for a volume-equivalent spherical bubble radius R for two selected η. This demonstrates favourable agreement of the volume dynamics in size and timing. The results also indicate that the bubble acquires a longer oscillation period as the distant wall moves closer to the proximal wall, i.e. for a more confined bubble.

Figure 2 compares the experimental and numerical bubble dynamics. The shadow images are experimental recordings, while the red contours superimposed are computed bubble interfaces at the same time instance. As well known, we find for small stand-off distance $\gamma = 0.47$ that the lower bubble wall flattens considerably and the bubble obtains a nearly hemispherical shape that later changes into a cone before collapsing as a toroidal bubble with a micro-jet impacting on the proximal wall. The bubble dynamics is rather weakly affected during the expansion and early shrinkage by the gap height η, see red and blue contours. Yet during collapse, the bubble develops a narrower apex during the collapse when the distance reduces to $\eta = 2.21$ (see $t = 140$ μs). This particular shape helps to build up a larger liquid pressure that accelerates the top bubble interface into a faster micro-jet. The computed velocity of the micro-jet $U_{jet} = 109.2$ m s^{-1} agrees well with the experimental measurement $U_{jet} = 95.6 \pm 24.3$ m s^{-1}. The jet velocity increases significantly from $U_{jet} = 71.9$ m s^{-1} for $\eta = 2.95$ to $U_{jet} = 109.2$ m s^{-1} for $\eta = 2.23$, which provides us with a robust method to enhance the micro-jet velocity.

Next, we concentrate on the jet formation process to develop a quantitative description of the micro-jet dynamics. Figure 3 compares the jet formation process for three selected gap heights of $H = 5$, 1.4 and 1.15 mm, respectively. Although the bubbles acquire similar outlines at their maximum expansion (see figure 2), the bubble's top surface behaves very differently during the collapse for various η. The main reason is that the pressure distribution varies with η at the maximum expansion. Since the flow between the bubble's apex and distant wall resembles a stagnation-point flow during the bubble's expansion, we analyse this flow with a potential flow coupled to a boundary-layer flow and to obtain the pressure difference between the bubble's top surface and the distant wall: $\Delta p = p_{wall} - p_b \sim k(H - R_{y,m})^2 + \mu f(y)$ (Schlichting & Gersten 2016), where p_{wall} and p_b are the pressures at the distant wall and bubble's top surface, $f(y)$ is a function accounting for the viscous boundary layer, $R_{y,m}$ the distance between the top surface and proximal wall that only slightly changes with η, $H - R_{y,m}$ is the distance from the bubble's top surface to the distant wall, and k is the coefficient. This pressure difference induces a pressure gradient that drives the bubble's top surface to move downwards once the collapse starts, which increases with H. Let's compare two cases $\eta = 8.42$ and $\eta = 2.00$. Figure 4 shows that the top surface of a bubble with a large distance $\eta = 8.42$ moves earlier and

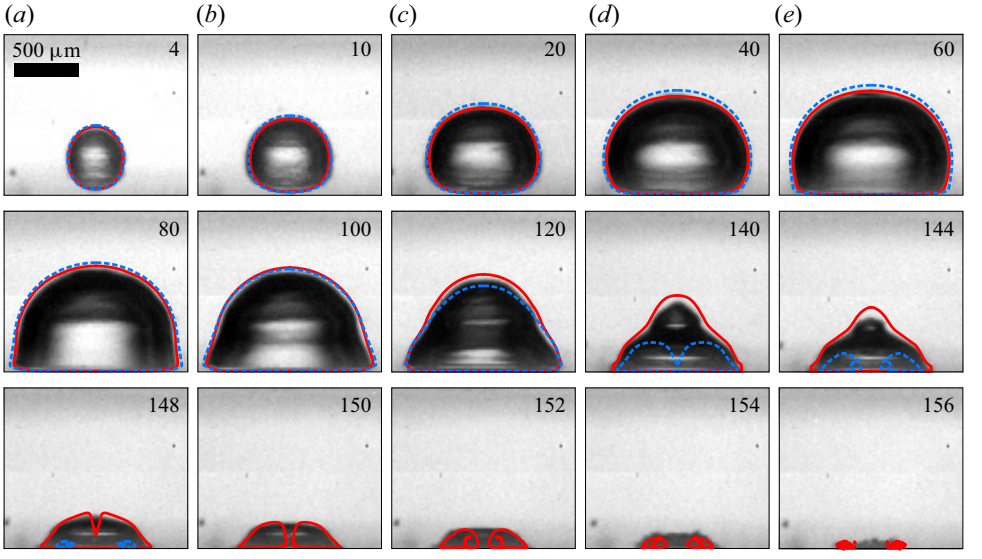

Figure 2. Comparison between experiments (background images) and simulation (red contours). Experiment, $R_{max} = 566 \pm 18$ μm, $d = 273 \pm 18$ μm, $H = 1260 \pm 18$ μm, $U_{jet} = 95.6 \pm 34.1$ m s^{-1}, $\gamma \approx 0.48$, $\eta \approx 2.23$; simulation, $R_{max} = 570.8$ μm, $d = 270$ μm, $H = 1260$ μm, $U_{jet} = 109.2$ m s^{-1}, $\gamma = 0.47$, $\eta = 2.21$, $p_0 = 946$ bar. The blue contours are computed bubble dynamics for a larger $\eta = 2.95$ but the same $\gamma = 0.47$, $U_{jet} = 71.9$ m s^{-1}. Numbers in the frames are time in microseconds.

reaches the bubble's bottom surface sooner, yet it has a slower final velocity of 64.3 m s^{-1}. Here y_{top} and U_{top} are the vertical postion and the vertical velocity of the bubble's top surface, respectively. For a smaller distance $\eta = 2.00$, the top surface moves slower at the beginning but is accelerated dramatically at approximately $t = 151$ μs and eventually develops a fast micro-jet with a speed of 280 m s^{-1}.

One may ask, why does the bubble with a small η move slower initially, but at the end develop a faster micro-jet? The mechanism is as follows. During the collapse, since the top surface is exposed to a smaller pressure gradient, the bubble shrinks faster in the annular direction, subsequently, this annular flow shapes the top surface into a conical shape, whose curvature $1/R_s$ increases with decreasing η (see figure 3). The annular flow meets on the axis of symmetry and is redirected downwards, which turns into a reverse stagnation-point flow that flows towards the conical shape (see sketch in figure 1(*b*) and local flow field in figure 3). As a result, hydrodynamic pressure builds up above the top surface. Once this pressure exceeds a threshold value, the flow starts to push the conical shape downwards. The convex interface then goes through a nearly flat shape and eventually develops as a jet at the axis. A straightforward comparison in figure 3 indicates that the bubble with a higher curvature acquires a larger pressure and therefore develops a faster micro-jet.

4. Micro-jet velocity

Next we determine the jet velocity U_{jet} to quantify the enhancement causing by the distant wall. Figure 5(*a*) compares U_{jet} as a function of η for 13 selected values of γ between 0.46 and 1.45. Again, we see favourable agreement of U_{jet} between experimental measurements and computed results for the large range of η studied. Our results show a similar trend for all γ that U_{jet} decreases dramatically with increasing η and eventually reaches a constant

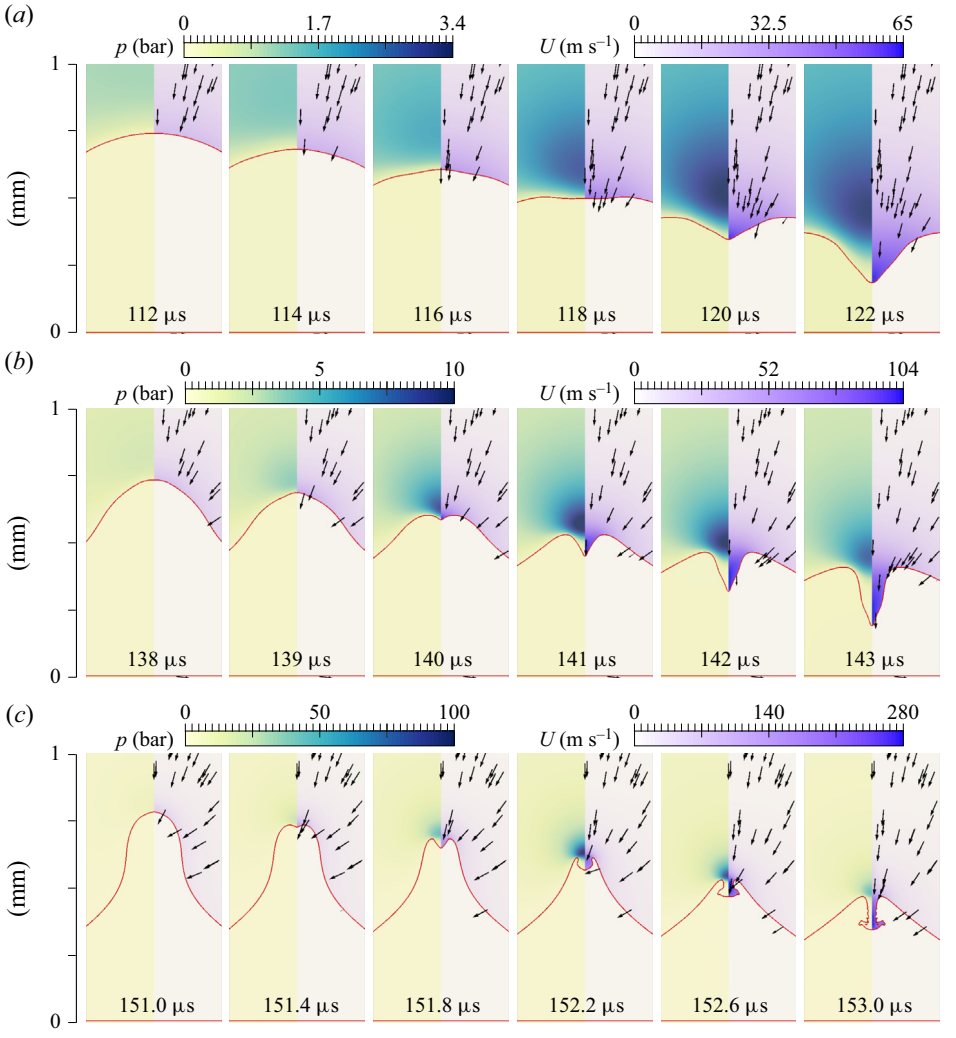

Figure 3. Jet formation for three selected cases with a constant $\gamma = 0.55$ but various η. (*a*) $H = 5$ mm, $\eta = 8.42$; (*b*) $H = 1.4$ mm, $\eta = 2.42$; (*c*) $H = 1.15$ mm, $\eta = 2.00$. All images focus on a region with a height of 1 mm and width of 0.5 mm. Red lines represent the bubble interfaces. The pressure and velocity magnitude are colour-coded on the left and right parts of each panel, respectively. Arrows indicate only the direction of the flow. Note the range of pressure and velocity for the colours are different for the three cases.

value. To determine an expression for the jet velocity, we start with an approximate acceleration on the bubble's top surface by simplifying the Navier–Stokes equation:

$$\frac{\mathrm{D}U}{\mathrm{D}t} = \frac{1}{\rho}\frac{p - p_b}{\delta}, \tag{4.1}$$

where δ is the distance between the bubble's top surface and the high pressure p location. Note that once the jet is formed, the acceleration drops dramatically as δ increases. Therefore, the acceleration is short-lived (see figures 3 and 4), and we expect the highest acceleration to occur immediately before the apex develops a concave shape. Below, we give an estimate for the driven pressure p_m at this instance of time. Assuming the

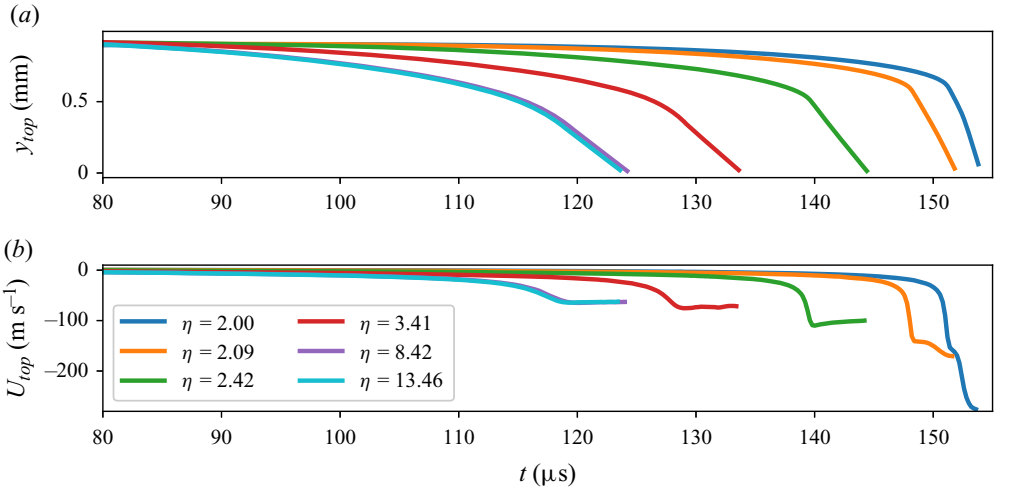

Figure 4. Comparison of the motion of the bubble's top surface for six selected η but constant $\gamma \approx 0.55$. (*a*) Position of top surfaces vs time. (*b*) Velocities of the top surfaces.

short-lived acceleration is increasing linearly, U_{jet} can be approximated as

$$U_{jet} \approx \frac{p_m \Delta t}{2\rho\delta}, \tag{4.2}$$

considering that the pressure $p_m \geqslant p_b$ and Δt is the duration of the pressure pulse. It is convenient to decompose the pressure into two parts $p_m \propto p_\infty + p_h$, where p_∞ and p_h are the pressure induced by the proximal and distant walls, respectively. For a certain γ, p_∞ generates a jet velocity U_∞ for $\eta \to \infty$ which is well studied in the literature; here we obtain an approximation of $U_\infty = 87.94\gamma^{0.5}$ for an ambient pressure of 1 atm. From figure 3 we observe that a relatively strong reverse stagnation-point flow impacting bubble's apex is formed due to the distant wall. Before jet formation the bubble's apex is hardly moved along the y direction, therefore applying potential flow theory p_m can be simplified to a hydrodynamic pressure caused by the flow with $p_h \sim \rho U_s^2$, where U_s is the additional flow velocity due to the distant wall. Next, we estimate U_s. The maximum boundary-layer thickness of the distant wall can be approximated to be of the order of $\sim \sqrt{\mu t_c/\rho} \approx 14$ μm with the collapse time t_c, therefore it is reasonable to apply the potential flow approximation where the velocity potential ϕ satisfies the Laplace equation $\nabla^2\phi = 0$. The solution for an axisymmetric stagnation-point flow is $U_r = ar$ and $U_y = -k(H - y)$, where a and k are the coefficients to be determined. For the cylindrical flow regime between the bubble's top surface and the distant wall, the flow is mostly downwards, therefore we can simplify the kinetic energy of this cylindrical flow as

$$\int_{R_y}^{H} \rho\pi R_s^2(-k(H-y))\,\mathrm{d}y \approx \frac{4}{3}\pi\Delta p(R_{max}^3 - R_t^3)\frac{R_s^2}{R_r^2}f, \tag{4.3}$$

where R_y is the vertical position of the bubble's top surface (see figure 1*b*), R_s is the radius of the bubble's apex, R_t the equivalent radius at time t, f is the vertical portion of the kinetic energy $(4/3)\pi\Delta p(R_{max}^3 - R_t^3)$ with $\Delta p = p_\infty - p_b \approx p_\infty$ (Lamb 1924); the right part of (4.3) also assumes the energy is proportional to area in the radial direction

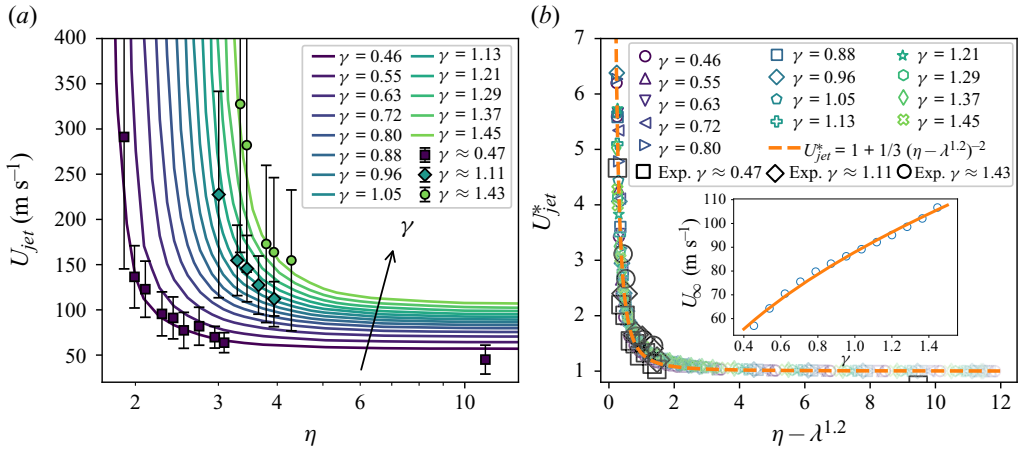

Figure 5. (*a*) Micro-jet velocities as a function of η. Solid lines are computed results for 13 selected values of γ between 0.46 and 1.45; black filled squares, diamonds and circles represent the experimental jet velocities for $\gamma \approx 0.47$, 1.11 and 1.43, respectively. A longitude scale for η is used to show better comparisons between different γ. (*b*) All data collapse onto an orange dashed line $U^*_{jet} = 1 + 1/3(\eta - \lambda^{1.2})^{-2}$, $U^*_{jet} = U_{jet}/U_\infty$ with U_∞ the jet velocity for $\eta \to \infty$ for a certain γ. Opacity from dark to light indicates increasing η. The inset depicts U_∞ as a function of γ; the orange solid line is $U_\infty = 87.94\gamma^{0.5}$ for an ambient pressure of 1 atm.

before the jet is formed, therefore a factor R_s^2/R_r^2 is applied, where R_r is the bubble's radial extension. At $r = 0$, $U_r = 0$ and $U_y = -k(H - R_y)$, thus together with (4.3) we find

$$p_h \sim \rho U_s^2 \approx \rho k^2 (H - R_y)^2 \sim \frac{4}{9}\pi\Delta p \left(\frac{R_{max}^3 - R_t^3}{R_r^2}\right)^2 (H - R_y)^{-2}. \tag{4.4}$$

Combining (4.2) and (4.4) and accounting for the time of acceleration $\Delta t \sim R_s(\rho/\Delta p)^{1/2}$, the jet velocity becomes

$$U_{jet} \sim \frac{2}{9}\left(\frac{H - R_y}{R_{max}}\right)^{-2} \frac{R_s}{\delta}\left(\frac{R_{max}^3 - R_t^3}{R_{max}R_r^2}\right)^2 \sqrt{\frac{\Delta p}{\rho}} + U_\infty. \tag{4.5}$$

Considering $U_\infty \sim \sqrt{\Delta p/\rho}$, and the fact that R_s and δ, R_{max} and R_r are of the same order of magnitude, respectively, we expect the jet velocity can be expressed as

$$U^*_{jet} = U_{jet}/U_\infty = 1 + a(\eta - \lambda^b)^{-2}, \tag{4.6}$$

with two proportionality factors a and b that we expect $a \sim O(0.1)$ and $b \sim O(1)$. Here, to relate R_y with the more easily accessible parameter $\lambda = R_{y,m}/R_{max}$, we introduce the proportionality factor b that accounts for the changing between $R_{y,m}$ and R_y and the effect of local curvature of the apex. We obtain $(a, b) = (1/3, 1.2)$ for all data (see figure 5*b*), and therefore the jet velocity under atmospheric pressure can be predicted as

$$U_{jet} = 87.94\gamma^{0.5}(1 + (1/3)(\eta - \lambda^{1.2})^{-2}). \tag{4.7}$$

5. Viscous effect

Viscosity is known to affect the boundary layer and induce viscous drag during the expanding and collapsing of a cavitation bubble. As a result, the jet formation and velocity

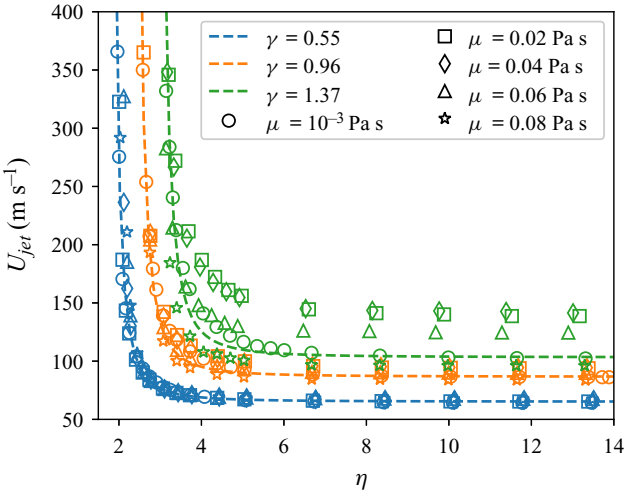

Figure 6. Comparison of U_{jet} as a function of η for bubbles with three selected γ and liquids of five different viscosities. Dashed lines are calculated using (4.7).

of a single wall-proximal bubble are highly influenced, too. Yet with an additional distant wall, we observe distinct fluid mechanics. Figure 6 compares the jet velocities for three selected stand-off distances $\gamma = 0.55$, 0.97 and 1.37, which are plotted with different colours. For each γ, we also compare the results of five viscosities indicated by different symbols. Overall, we observe a rapid reduction of the jet velocity as η increases, which indicates that the distant wall still holds a significant impact on U_{jet} even for liquids with high viscosities.

Looking closer into the data, we find that for small stand-off distance $\gamma = 0.55$, the data for all viscosities collapse onto the theoretical curve $U_{jet} = 87.94\gamma^{0.5}(1 + (1/3)(\eta - (1+\gamma)^{1.2})^{-2})$. Here $\lambda \approx 1 + \gamma$ (Reuter, Zeng & Ohl 2022). The result suggests that the jet formation is still dominated by the geometry, i.e. by the proximal and distant walls. Within this particular regime, a thin liquid film occurs between the bubble's lower surface and the proximal wall h, which ensures the bubble's lower wall is trapped. Except for the lower interface, the viscous drag that acts on all collapsing parts of the bubble's surface is proportional to μ; as a result the relative motion remains, and the distant wall holds the same role in building up the high pressure to drive the bubble's apex, thus (4.7) remains appropriate.

When γ increases to 0.97, our result shows that for small $\eta < 3$ the jet velocities still conform well to (4.7), implying the dominance of the geometry remains. Yet for large $\eta > 3$ the results display a more scattered distribution and deviate from the theoretical prediction. This is due to the increase in the liquid-film thickness h between the bubble's lower surface and the proximal wall (Zeng *et al.* 2022), resulting in a greater motion of the lower-bubble interface during the collapse. Here, a thicker viscous boundary layer on the proximal wall results in a more complex vertical motion of the bubble. This may explain the scatter of the data for U_{jet} below 150 m s^{-1}.

For a large stand-off distance $\gamma = 1.37$, viscosity not only slows down the bubble's motion but also helps to form complex structures. Unexpectedly large curvatures at the bubble apex are known to be formed due to a combined effect of viscous drag and the collapsing flow, which results in the occurrence of higher velocity jets in a more viscous liquid (Zeng *et al.* 2022). Here we measure higher velocities for liquids with viscosities

$\mu = 0.02$ Pa s, $\mu = 0.04$ Pa s and $\mu = 0.06$ Pa s as compared with water. As viscosity increases to $\mu = 0.08$ Pa s, the large viscous drag forces the bubble surface to a convex and smooth shape, thereby decreasing the jet velocity.

6. Conclusion

In summary, a distant wall is found to enhance the jetting from a collapsing wall-proximal cavitation bubble. Combining high-speed photography and compressible VoF simulations, we find that the distant wall influences the micro-jet by converting the collapsing flow into a stagnation-point flow that drives the bubble's top surface. This flow, which changes dramatically for small η but becomes constant for relatively large η, builds up a high pressure that drives the bubble's top surface to collapse into micro-jet. We derive a formula for the jet velocity of $U_{jet} = 87.94\gamma^{0.5}(1 + (1/3)(\eta - \lambda^{1.2})^{-2})$, which correctly predicts our experimental and simulation results. Although viscosity affects the bubble dynamics in a rather complex way, the jet velocity for small γ is found to still follow the above-derived equation, where geometric effects dominate the collapsing flow.

Acknowledgements. The anonymous referees are acknowledged for their very helpful suggestions to improve the manuscript.

Funding. This research was partly funded by the National Natural Science Foundation of China under grant nos. 51925904 and 12302313, the Fundamental Research Funds for the Central Universities of Ministry of Education of China under grant no. 3072023CFJ0105, the Finance Science and Technology Project of Hainan Province under grant no. ZDKJ2021020, the Australian Research Council Discovery Project under grant no. DP230100556 and the Deutsche Forschungsgemeinschaft (DFG, German Research Foundation) under grant no. DE 3156/6-1.

Declaration of interests. The authors report no conflict of interest.

Author ORCIDs.
Qingyun Zeng https://orcid.org/0000-0003-1369-8236;
A-Man Zhang https://orcid.org/0000-0003-1299-3049;
Claus-Dieter Ohl https://orcid.org/0000-0001-5333-4723.

References

BRACKBILL, J.U., KOTHE, D.B. & ZEMACH, C. 1992 A continuum method for modeling surface tension. *J. Comput. Phys.* **100** (2), 335–354.

DIJKINK, R. & OHL, C.-D. 2008 Measurement of cavitation induced wall shear stress. *Appl. Phys. Lett.* **93** (25), 254107.

GONZALEZ-AVILA, S.R., VAN BLOKLAND, A.C., ZENG, Q. & OHL, C.-D. 2020 Jetting and shear stress enhancement from cavitation bubbles collapsing in a narrow gap. *J. Fluid Mech.* **884**, A23.

HAN, B., KÖHLER, K., JUNGNICKEL, K., METTIN, R., LAUTERBORN, W. & VOGEL, A. 2015 Dynamics of laser-induced bubble pairs. *J. Fluid Mech.* **771**, 706–742.

KOCH, M., LECHNER, C., REUTER, F., KÖHLER, K., METTIN, R. & LAUTERBORN, W. 2016 Numerical modeling of laser generated cavitation bubbles with the finite volume and volume of fluid method, using openfoam. *Comput. Fluids* **126**, 71–90.

LAMB, H. 1924 *Hydrodynamics*. University Press.

LAUTERBORN, W. & BOLLE, H. 1975 Experimental investigations of cavitation-bubble collapse in the neighbourhood of a solid boundary. *J. Fluid Mech.* **72** (2), 391–399.

LECHNER, C., LAUTERBORN, W., KOCH, M. & METTIN, R. 2020 Jet formation from bubbles near a solid boundary in a compressible liquid: numerical study of distance dependence. *Phys. Rev. Fluids* **5** (9), 093604.

OGASAWARA, T., TSUBOTA, N., SEKI, H., SHIGAKI, Y. & TAKAHIRA, H. 2015 Experimental and numerical investigations of the bubble collapse at the center between rigid walls. In *Journal of Physics: Conference Series* (ed. M. Farhat & A. Müller), vol. 656, p. 012031. IOP Publishing.

PLESSET, M.S. & CHAPMAN, R.B. 1971 Collapse of an initially spherical vapour cavity in the neighbourhood of a solid boundary. *J. Fluid Mech.* **47** (2), 283–290.

REESE, H., SCHADEL, R., REUTER, F. & OHL, C.-D. 2022 Microscopic pumping of viscous liquids with single cavitation bubbles. *J. Fluid Mech.* **944**, A17.

REUTER, F., GONZALEZ-AVILA, S.R., METTIN, R. & OHL, C.-D. 2017 Flow fields and vortex dynamics of bubbles collapsing near a solid boundary. *Phys. Rev. Fluids* **2**, 064202.

REUTER, F. & OHL, C.-D. 2021 Supersonic needle-jet generation with single cavitation bubbles. *Appl. Phys. Lett.* **118** (13), 134103.

REUTER, F., ZENG, Q. & OHL, C.-D. 2022 The Rayleigh prolongation factor at small bubble to wall stand-off distances. *J. Fluid Mech.* **944**, A11.

ROSSELLÓ, J.M., LAUTERBORN, W., KOCH, M., WILKEN, T., KURZ, T. & METTIN, R. 2018 Acoustically induced bubble jets. *Phys. Fluids* **30** (12), 122004.

RUSCHE, H. 2003 Computational fluid dynamics of dispersed two-phase flows at high phase fractions. PhD thesis, Imperial College London.

SCHLICHTING, H. & GERSTEN, K. 2016 *Boundary-Layer Theory*. Springer.

SEKI, H., FUJITA, K., OGASAWARA, T. & TAKAHIRA, H. 2015 Numerical simulations of growth and collapse of a bubble between two parallel walls. In *Fluids Engineering Division Summer Meeting*, vol. 57230, p. V02AT05A004. ASME.

TALEGHANI, M.H., KHODADADI, S., MADDAHIAN, R. & MOKHTARI-DIZAJI, M. 2023 Enhancing the bubble collapse energy using the electrohydrodynamic force. *Phys. Fluids* **35** (5), 053316.

ZENG, Q., AN, H. & OHL, C.-D. 2022 Wall shear stress from jetting cavitation bubbles: influence of the stand-off distance and liquid viscosity. *J. Fluid Mech.* **932**, A14.

ZENG, Q., GONZALEZ-AVILA, S.R. & OHL, C.-D. 2020 Splitting and jetting of cavitation bubbles in thin gaps. *J. Fluid Mech.* **896**, A28.

ZENG, Q., GONZALEZ-AVILA, S.R., TEN VOORDE, S. & OHL, C.-D. 2018 Jetting of viscous droplets from cavitation-induced Rayleigh–Taylor instability. *J. Fluid Mech.* **846**, 916–943.

ZHANG, A., LI, S., CUI, P., LI, S. & LIU, Y. 2023 A unified theory for bubble dynamics. *Phys. Fluids* **35** (3), 033323.